INTERNATIONAL JOURNAL FOR NUMERICAL METHODS IN FLUIDS
Int. J. Numer. Meth. Fluids 2009; **60**:337–353
Published online 24 September 2008 in Wiley InterScience (www.interscience.wiley.com). DOI: 10.1002/fld.1899

SHORT COMMUNICATION

A numerical technique for laminar swirling flow at the interface between porous and homogenous fluid domains

P. Yu[1,2,*,†], T. S. Lee[1], Y. Zeng[1], S. A. Meguid[2] and H. T. Low[3]

[1]*Department of Mechanical Engineering, National University of Singapore, Singapore, Singapore*
[2]*School of Mechanical & Aerospace Engineering, Nanyang Technological University, Singapore, Singapore*
[3]*Division of Bioengineering, National University of Singapore, Singapore, Singapore*

SUMMARY

There have been a few recent numerical implementations of the stress-jump condition at the interface of conjugate flows, which couple the governing equations for flows in the porous and homogenous fluid domains. These previous demonstration cases were for two-dimensional, planar flows with simple geometries, for example, flow over a porous layer or flow through a porous plug. The present study implements the interfacial stress-jump condition for a non-planar flow with three velocity components, which is more realistic in terms of practical flow applications. The steady, laminar, Newtonian flow in a stirred micro-bioreactor with a porous scaffold inside was investigated. It is shown how to implement the interfacial jump condition on the radial, axial, and swirling velocity components. To avoid a full three-dimensional simulation, the flow is assumed to be independent of the azimuthal direction, which makes it an axisymmetric flow with a swirling velocity. The present interface treatment is suitable for non-flat surfaces, which is achieved by applying the finite volume method based on body-fitted and multi-block grids. The numerical simulations show that a vortex breakdown bubble, attached to the free surface, occurs above a certain Reynolds number. The presence of the porous scaffold delays the onset of vortex breakdown and confines it to a region above the scaffold. Copyright © 2008 John Wiley & Sons, Ltd.

Received 21 June 2007; Revised 8 July 2008; Accepted 14 July 2008

KEY WORDS: swirling flow; porous–fluid interface; stress jump; porous medium; block-structured grids; tissue-engineering scaffold

1. INTRODUCTION

Flows in porous media are of importance in many engineering applications, including tissue-engineering scaffolds in bioreactors, polymeric micro-spheres for drug delivery, porous heat sink

*Correspondence to: P. Yu, Department of Mechanical Engineering, National University of Singapore, 9 Engineering Drive 1, Singapore 117576, Singapore.
†E-mail: mpeyp@nus.edu.sg

for enhanced heat transfer, etc. Such applications involve flows in two regions: homogenous fluid and porous medium. To solve such flows, the numerical approaches are based on one or two domains. In the two-domain approach, two sets of governing equations are needed to model the flows in the two regions, and to couple the equations, additional interfacial boundary conditions are required.

Different boundary conditions at the interface have been proposed: semi-empirical slip boundary condition [1], continuous boundary conditions in both stress and velocity [2], and stress-jump conditions [3–5]. Among which, the shear jump condition [3, 4] has been widely applied. For example, Kuznetsov [6–8] applied it for analytical investigation of flow in channel partially filled with porous medium and Partha *et al.* [9] employed it for viscous flow past a porous spherical shell. Goyeau *et al.* [10] have introduced a transition layer between porous–fluid regions to derive an explicit function of the stress-jump coefficient. Chandesris and Jamet [11, 12] have proposed a two-step up-scaling method to estimate the jump coefficients for the stress-jump conditions. The different interfacial conditions were found to have more effect on the velocity field and less effect on the temperature field or Nusselt number distribution [13].

Associated with the different interface conditions, numerical techniques to solve the coupled flows have been developed. Slip velocity and continuity of both velocity and stress conditions were used by Gartling *et al.* [14]. Continuity of both velocity and stress condition was used by Costa *et al.* [15] and Betchen *et al.* [16]. The stress-jump condition was used by Silva and de Lemos [17].

Recently, Yu *et al.* [18] developed a numerical methodology using the finite volume method, based on a collocated variable arrangement, to treat the stress-jump condition given by Ochoa-Tapia and Whitaker [5], which includes the inertial effects. By combining body-fitted and multi-block grids, the numerical technique of Yu *et al.* [18] is effective in simulating the coupled flow in the homogeneous fluid and porous medium regions involving complex geometries. The general method was applied to solve three flow configurations: flow over a porous layer, flow through a porous plug, and flow past a porous square cylinder. However, the technique is restricted to planar flows with two velocity components, which are different from those of practical applications, such as a stirred bioreactor with medium swirling around porous scaffolds.

Sucosky *et al.* [19] experimentally and numerically investigated the flow around and through tissue-engineered cartilage constructs in a spinner-flask bioreactor agitated by a magnetic stir bar. The commercial software FLUENT was used to simulate the flow field by assuming the cartilage constructs as impermeable structures. Once the pressures on the assumed-solid construct surface were determined, a porous flow model based on Darcy's law was applied to predict the volume-flow rate of culture medium through the porous construct. That is, the flows in the fluid medium and porous scaffold were not coupled.

Of related interest to flow in a stirred bioreactor with porous scaffolds is the study by Yu *et al.* [18], mentioned earlier, on two-dimensional flow past a porous square cylinder. However, the flow in a stirred bioreactor system is much more complicated as it is three dimensional. The flow behavior is largely influenced by the swirling velocity component, which may result in vortex breakdown, as observed experimentally by Dusting *et al.* [20]. The phenomenon is related to that of swirling flow and vortex breakdown in a chamber of which there have been many previous studies [21–23], but so far these did not consider a porous medium inside.

The objective of the present work is to implement the interfacial stress-jump condition for a non-planar flow with three velocity components. As a demonstration case, the steady, laminar, Newtonian flow in a stirred micro-bioreactor with a porous scaffold inside is investigated. The system, resembling that of Dusting *et al.* [20], consists of an open cylinder chamber filled with

DOI: 10.1002/fld

culture medium, which is stirred by a rotating bottom-wall. To avoid a full three-dimensional simulation, the flow is assumed to be independent of the azimuthal direction, which reduces it to an axisymmetric flow with a swirling velocity. The present numerical implementation of the jump condition is a continuation of the previous one for planar flows with two velocity components [18].

2. GOVERNING EQUATIONS AND BOUNDARY CONDITIONS

The micro-bioreactor with a tissue-engineering scaffold is shown schematically in Figure 1(a). The bioreactor consists of a cylindrical chamber filled with culture medium. The culture medium is considered as a Newtonian fluid. The medium mixing is generated by the rotating bottom-wall. In cell culture application, the dynamic viscosity and density of the culture medium are around $10^{-3}\,\mathrm{m^2\,s^{-1}}$ and $10^{3}\,\mathrm{kg\,m^{-3}}$, respectively. A typical rotating speed of the bottom-wall is around 150 rpm.

The scaffold with a concentric hole is coaxially mounted in the bioreactor. The porosity of the scaffold is in the range of 0.6–0.95 [24, 25] and the permeability of the scaffold is in the range of 10^{-12}–$10^{-9}\,\mathrm{m^2}$ [26, 27]. As the bioreactor and scaffold can be regarded as two concentric cylinders, the geometry is axisymmetric. The computational domain for the bioreactor with the scaffold is shown in Figure 1(b) and an example of the domain partitioning and grid topology is shown in Figure 1(c).

For a typical application, a case was considered in which the height of the bioreactor H was 10 mm and the radius R was 10 mm. It was assumed that the thickness of the scaffold was 2 mm and the diameter was 12 mm. The diameter of the hole was 3 mm. The scaffold was fixed at the 60% height of the bioreactor. The detailed geometric parameters in Figure 1(b) were summarized in Table I.

The scaffold could be considered as a porous medium. Thus, the flow in a stirred bioreactor with scaffold is a typical system of swirling flow, which contains an interface between porous medium and homogenous fluid. The governing equations for a steady axisymmetric laminar flow of an incompressible viscous Newtonian fluid in the homogenous fluid region are expressed as

$$\frac{1}{r}\frac{\partial(rv_r)}{\partial r}+\frac{\partial v_z}{\partial z}=0 \tag{1}$$

$$\frac{1}{r}\frac{\partial(rv_rv_z)}{\partial r}+\frac{\partial(v_zv_z)}{\partial z}=-\frac{1}{\rho}\frac{\partial p}{\partial z}+\frac{\mu}{\rho}\left[\frac{1}{r}\frac{\partial}{\partial r}\left(r\frac{\partial v_z}{\partial r}\right)+\frac{\partial^2 v_z}{\partial z^2}\right] \tag{2}$$

$$\frac{1}{r}\frac{\partial(rv_rv_r)}{\partial r}+\frac{\partial(v_zv_r)}{\partial z}=-\frac{1}{\rho}\frac{\partial p}{\partial r}+\frac{\mu}{\rho}\left[\frac{\partial}{\partial r}\left(\frac{1}{r}\frac{\partial}{\partial r}(rv_r)\right)+\frac{\partial^2 v_r}{\partial z^2}\right]+\frac{v_\theta^2}{r} \tag{3}$$

$$\frac{1}{r}\frac{\partial(rv_rv_\theta)}{\partial r}+\frac{\partial(v_zv_\theta)}{\partial z}=\frac{\mu}{\rho}\left[\frac{\partial}{\partial r}\left(\frac{1}{r}\frac{\partial}{\partial r}(rv_\theta)\right)+\frac{\partial^2 v_\theta}{\partial z^2}\right]-\frac{v_rv_\theta}{r} \tag{4}$$

where v_r, v_z, and v_θ are the radial, axial, and azimuthal velocities, respectively; r and z are the radial and axial coordinates, respectively; p is the pressure; ρ is the mass density of the fluid; and μ is the fluid dynamic viscosity.

DOI: 10.1002/fld

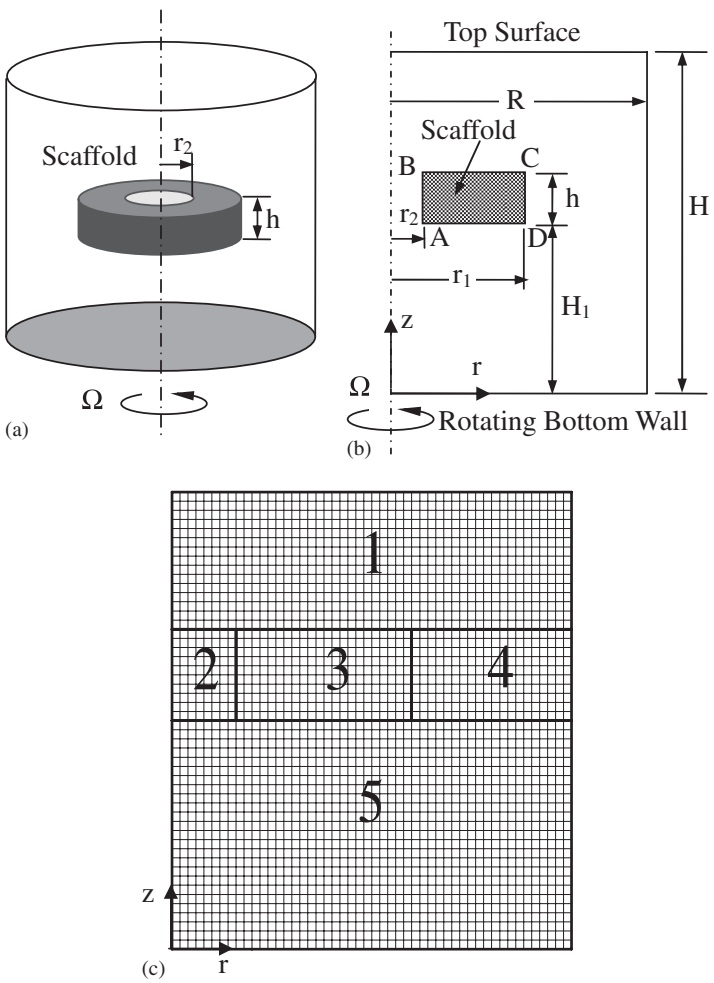

Figure 1. Bioreactor system with a tissue-engineering scaffold: (a) schematic; (b) computational domain; and (c) domain partitioning and grid topology; a large grid size was chosen to clearly demonstrate the grid topology.

Table I. Geometric parameters for the computational domain.

	R	H	H_1	h	r_1	r_2
Size (mm)	10	10	5	2	1.5	6

The porous medium is considered to be rigid, homogeneous, and isotropic and is saturated with the same single-phase fluid as that in the homogenous fluid region. Considering viscous and inertial effects, the governing equations for the flow in the porous region, based on

DOI: 10.1002/fld

Darcy–Brinkman–Forchheimer extended model, can be expressed as [28, 29]

$$\frac{1}{r}\frac{\partial(rv_r)}{\partial r}+\frac{\partial v_z}{\partial z}=0 \tag{5}$$

$$\frac{1}{r}\frac{\partial}{\partial r}\left(\frac{rv_rv_z}{\varepsilon}\right)+\frac{\partial}{\partial z}\left(\frac{v_zv_z}{\varepsilon}\right)=-\frac{1}{\rho}\frac{\partial(\varepsilon p^*)}{\partial z}+\frac{\mu}{\rho}\left[\frac{1}{r}\frac{\partial}{\partial r}\left(r\frac{\partial v_z}{\partial r}\right)+\frac{\partial^2 v_z}{\partial z^2}\right]-\frac{\varepsilon v_rv_z}{r}$$
$$-\frac{\mu\varepsilon}{\rho K}v_z-\frac{\varepsilon C_{\mathrm{F}}\sqrt{v_z^2+v_r^2+v_\theta^2}}{\sqrt{K}}v_z \tag{6}$$

$$\frac{1}{r}\frac{\partial}{\partial r}\left(\frac{rv_rv_r}{\varepsilon}\right)+\frac{\partial}{\partial z}\left(\frac{v_zv_r}{\varepsilon}\right)=-\frac{1}{\rho}\frac{\partial(\varepsilon p^*)}{\partial r}+\frac{\mu}{\rho}\left[\frac{\partial}{\partial r}\left(\frac{1}{r}\frac{\partial}{\partial r}(rv_r)\right)+\frac{\partial^2 v_r}{\partial z^2}\right]+\frac{\varepsilon v_\theta^2}{r}$$
$$-\frac{\mu\varepsilon}{\rho K}v_r-\frac{\varepsilon C_{\mathrm{F}}\sqrt{v_z^2+v_r^2+v_\theta^2}}{\sqrt{K}}v_r \tag{7}$$

$$\frac{1}{r}\frac{\partial}{\partial r}\left(\frac{rv_rv_\theta}{\varepsilon}\right)+\frac{\partial}{\partial z}\left(\frac{v_zv_\theta}{\varepsilon}\right)=\frac{\mu}{\rho}\left[\frac{\partial}{\partial r}\left(\frac{1}{r}\frac{\partial}{\partial r}(rv_\theta)\right)+\frac{\partial^2 v_\theta}{\partial z^2}\right]-\frac{\varepsilon v_rv_\theta}{r}$$
$$-\frac{\mu\varepsilon}{\rho K}v_\theta-\frac{\varepsilon C_{\mathrm{F}}\sqrt{v_z^2+v_r^2+v_\theta^2}}{\sqrt{K}}v_\theta \tag{8}$$

where p^* is the intrinsic average pressure, μ is the fluid dynamic viscosity, ε is the porosity, K is the permeability, and C_{F} is the Forchheimer coefficient. Note that throughout the paper, viscosity means dynamic viscosity of the fluid but not the effective (Brinkman) viscosity. The velocity components v_r, v_z, and v_θ in porous region are the local average velocity (Darcy velocity). The superscript '*' denotes the intrinsic average. The local average and intrinsic average can be linked by the Dupuit–Forchheimer relationship, for example, $p=\varepsilon p^*$.

To solve Equations (1)–(8), the appropriate boundary conditions are imposed at the interface between the homogenous fluid and porous medium regions. The continuity of velocity components at the interface is given by

$$v_r|_{\mathrm{fluid}}=v_r|_{\mathrm{porous}}=v_r|_{\mathrm{interface}} \tag{9}$$

$$v_z|_{\mathrm{fluid}}=v_z|_{\mathrm{porous}}=v_z|_{\mathrm{interface}} \tag{10}$$

$$v_\theta|_{\mathrm{fluid}}=v_\theta|_{\mathrm{porous}}=v_\theta|_{\mathrm{interface}} \tag{11}$$

The shear stress-jump condition [5] and the continuity of the normal stress at the interface can be expressed as

$$\frac{\mu}{\varepsilon}\frac{\partial v_t}{\partial n}\bigg|_{\mathrm{porous}}-\mu\frac{\partial v_t}{\partial n}\bigg|_{\mathrm{fluid}}=\beta_1\frac{\mu}{\sqrt{K}}v_t\bigg|_{\mathrm{interface}}+\beta_2\rho v_t^2\bigg|_{\mathrm{interface}} \tag{12}$$

DOI: 10.1002/fld

$$\left.\frac{\mu}{\varepsilon}\frac{\partial v_n}{\partial n}\right|_{\text{porous}} - \left.\mu\frac{\partial v_n}{\partial n}\right|_{\text{fluid}} = 0 \tag{13}$$

where n is a coordinate normal to the interface with its direction from porous medium to homogenous fluid, v_n is the velocity component perpendicular to the interface, t is a coordinate perpendicular to n with its direction determined by the right-handed system, v_t is the velocity component tangential to the interface, and β_1 is a coefficient associated with an excess viscous stress, whereas β_2 is a coefficient related to an excess inertial stress. Note that the stress-jump condition is based on a generalized non-local form of the volume average Navier–Stokes equations, which accounts for the excess surface stress encountered at the interface. Ochoa-Tapia and Whitaker's experiment [4] and analysis [5] indicated that both β_1 and β_2 are of order 1. In the present study, the jump parameters β_1 and β_2 were set to 0.7 and 0, respectively, unless otherwise specified.

The non-slip boundary condition is imposed on the solid wall, that is

$$v_r = 0, \quad v_z = 0, \quad v_\theta = 0 \quad \text{on stationary side-wall} \tag{14}$$

$$v_r = 0, \quad v_z = 0, \quad v_\theta = \Omega r \quad \text{on rotating bottom-wall} \tag{15}$$

The deformation of the free surface due to the rotation of the fluid is proportional to the Froude number, which is defined as

$$Fr = \Omega^2 R^2 / gH \tag{16}$$

where g is the gravitational constant. Since the Reynolds number was less than 1500, the Froude number Fr was negligibly small (in the order of 10^{-3}) and the free surface was assumed to be a flat stress-free surface. This assumption has been applied by other researchers to investigate the swirling flow in a chamber with a free surface [21].

The length and velocity components were scaled by $1/R$ and $1/(\Omega R)$, respectively. The Reynolds number is defined as $Re = \rho\Omega R^2/\mu$. The Reynolds number was kept within 1500 to ensure steady flow condition. The Darcy number is defined as $Dar = K/R^2$. The aspect ratio was fixed at $H/R = 1.0$.

3. DISCRETIZATION

To solve the above equations, a finite volume method with a collocated variable arrangement was used. It is based on non-orthogonal (body-fitted) grids, although the grid topology in Figure 1(c) has a quite regular configuration. In fact, the surface vector of control volume may not be parallel or normal to the velocity components in the present method. Thus, all the velocity components contribute to the mass flux, which is the sum of the products of each Cartesian velocity component multiplied by the corresponding surface vector component. The present numerical method has been successfully applied for both swirling follow problems [22, 23] and the coupled problems involving both porous medium and homogenous fluid regions [18, 30]. The detailed discretization procedure can be found in [18, 31] and a brief outline is described here.

The central difference scheme was used to approximate the value of the variable and its derivative at the cell face. The midpoint rule with the deferred correction term [32] was applied to integrate the diffusive flux. The SIMPLEC method [33] was applied to couple the velocity and pressure. To avoid oscillations in the pressure or velocity, the interpolation proposed by Rhie and Chow [34]

DOI: 10.1002/fld

was adopted. For v_θ equation, as there is no pressure term, it can be treated as a conservation equation for a general dependent variable.

Figure 2 shows details of the interface between two different blocks. The neighboring control volumes lying in grid-blocks A and B share the interface and the grids in these two neighboring blocks match at that interface. There are three types of interfaces when the block-structured grid method is employed to calculate the flow in the composite region: (i) fluid–fluid interface, (ii) porous medium–porous medium interface, and (iii) porous medium–fluid interface.

When both blocks A and B (Figure 2) represent the same media, either fluid or porous medium, the method proposed by Lilek *et al.* [35] was applied to treat the block interface. When blocks A and B (Figure 2) represent fluid and porous medium, respectively, the velocity vector at the

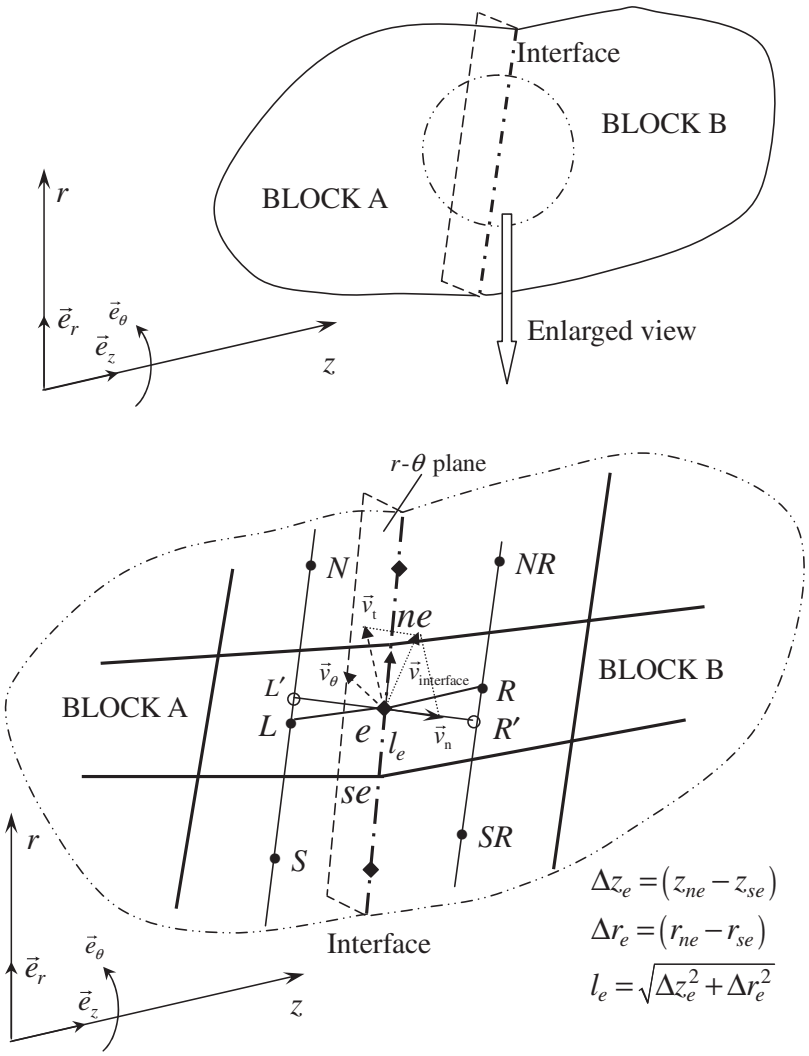

Figure 2. Interface between two blocks with matching grids.

DOI: 10.1002/fld

interface $\mathbf{v}_{\text{interface}}$ can be expressed as

$$\mathbf{v}_{\text{interface}} = v_r\mathbf{e}_r + v_z\mathbf{e}_z + v_\theta\mathbf{e}_\theta = v_n\mathbf{n} + v_t\mathbf{t} \tag{17}$$

where $\mathbf{n}$ is a unit vector normal to the interface with its direction from porous medium to homogenous fluid and $\mathbf{t}$ is a unit vector tangent to the interface. By combining Equations (12), (13), and (15)

$$\frac{\mu}{\varepsilon}\frac{\partial \mathbf{v}_{\text{interface}}}{\partial n}\bigg|_{\text{porous}} - \mu\frac{\partial \mathbf{v}_{\text{interface}}}{\partial n}\bigg|_{\text{fluid}} = \beta_1\frac{\mu}{\sqrt{K}}v_t\mathbf{t} + \beta_2\rho v_t^2\mathbf{t} \tag{18}$$

For the condition without azimuthal velocity, the unit tangent vector $\mathbf{t}$ is within the r–z plane and can be calculated as [18]

$$\mathbf{t} = \frac{\Delta r\mathbf{e}_r + \Delta z\mathbf{e}_z}{l} \tag{19}$$

However, for the swirling flow problem, the azimuthal velocity has contribution to the tangent velocity v_t. Thus, the unit tangent vector $\mathbf{t}$ (Figure 2) is not within the r–z plane and should be calculated from

$$\mathbf{t} = \frac{\left(\dfrac{v_r\Delta r + v_z\Delta z}{l}\right)\left(\dfrac{\Delta r\mathbf{e}_r + \Delta z\mathbf{e}_z}{l}\right) + v_\theta\mathbf{e}_\theta}{\sqrt{\left(\dfrac{v_r\Delta r + v_z\Delta z}{l}\right)^2 + v_\theta^2}} \tag{20}$$

And v_t then can be expressed as

$$v_t = (v_r\mathbf{e}_r + v_z\mathbf{e}_z + v_\theta\mathbf{e}_\theta)\cdot\mathbf{t} = \sqrt{\left(\frac{v_r\Delta r + v_z\Delta z}{l}\right)^2 + v_\theta^2} \tag{21}$$

By substituting the components of $\mathbf{v}_{\text{interface}}$ in z, r, and θ directions and combining Equations (18) and (19), Equation (16) becomes

$$\begin{aligned}
&\frac{\mu}{\varepsilon}\frac{\partial[v_r\mathbf{e}_r + v_z\mathbf{e}_z + v_\theta\mathbf{e}_\theta]}{\partial n}\bigg|_{\text{porous}} - \mu\frac{\partial[v_r\mathbf{e}_r + v_z\mathbf{e}_z + v_\theta\mathbf{e}_\theta]}{\partial n}\bigg|_{\text{fluid}} \\
&\quad = \beta_1\frac{\mu}{\sqrt{K}}\left[\left(\frac{v_r\Delta r + v_z\Delta z}{l}\right)\left(\frac{\Delta r\mathbf{e}_r + \Delta z\mathbf{e}_z}{l}\right) + v_\theta\mathbf{e}_\theta\right] \\
&\qquad + \beta_2\rho\sqrt{\left(\frac{v_r\Delta r + v_z\Delta z}{l}\right)^2 + v_\theta^2}\left[\left(\frac{v_r\Delta r + v_z\Delta z}{l}\right)\left(\frac{\Delta r\mathbf{e}_r + \Delta z\mathbf{e}_z}{l}\right) + v_\theta\mathbf{e}_\theta\right]
\end{aligned} \tag{22}$$

Equation (20) can be rewritten as

$$\begin{aligned}
\frac{\mu}{\varepsilon}\frac{\partial v_z}{\partial n}\bigg|_{\text{porous}} - \mu\frac{\partial v_z}{\partial n}\bigg|_{\text{fluid}} &= \beta_1\frac{\mu}{\sqrt{K}}\frac{v_z\Delta z\Delta z + v_r\Delta r\Delta z}{l^2} \\
&\quad + \beta_2\rho\frac{v_z\Delta z\Delta z + v_r\Delta r\Delta z}{l^2}\sqrt{\left(\frac{v_r\Delta r + v_z\Delta z}{l}\right)^2 + v_\theta^2}
\end{aligned} \tag{23}$$

DOI: 10.1002/fld

$$\left.\frac{\mu}{\varepsilon}\frac{\partial v_r}{\partial n}\right|_{\text{porous}} - \left.\mu\frac{\partial v_r}{\partial n}\right|_{\text{fluid}} = \beta_1\frac{\mu}{\sqrt{K}}\frac{v_z\Delta z\Delta r + v_r\Delta r\Delta r}{l^2} + \beta_2\rho\frac{v_z\Delta z\Delta r + v_r\Delta r\Delta r}{l^2}\sqrt{\left(\frac{v_r\Delta r + v_z\Delta z}{l}\right)^2 + v_\theta^2} \tag{24}$$

$$\left.\frac{\mu}{\varepsilon}\frac{\partial v_\theta}{\partial n}\right|_{\text{porous}} - \left.\mu\frac{\partial v_\theta}{\partial n}\right|_{\text{fluid}} = \beta_1\frac{\mu}{\sqrt{K}}v_\theta + \beta_2\rho v_\theta\sqrt{\left(\frac{v_r\Delta r + v_z\Delta z}{l}\right)^2 + v_\theta^2} \tag{25}$$

The derivatives at the interface are calculated from the values at auxiliary nodes L' and R'; these nodes lie at the intersection of the cell face normal n and straight lines connecting nodes L and N or R and NR, respectively (Figure 2). The normal gradients at the interface can be calculated by using the first-order difference approximation:

$$\left.\frac{\partial v_r}{\partial n}\right|_{\text{porous}} = \frac{v_r|_{R'} - v_r|_e}{L_{eR'}}, \quad \left.\frac{\partial v_z}{\partial n}\right|_{\text{porous}} = \frac{v_z|_{R'} - v_z|_e}{L_{eR'}}, \quad \left.\frac{\partial v_\theta}{\partial n}\right|_{\text{porous}} = \frac{v_\theta|_{R'} - v_\theta|_e}{L_{eR'}} \tag{26}$$

$$\left.\frac{\partial v_r}{\partial n}\right|_{\text{fluid}} = \frac{v_r|_e - v_r|_{L'}}{L_{L'e}}, \quad \left.\frac{\partial v_z}{\partial n}\right|_{\text{fluid}} = \frac{v_z|_e - v_z|_{L'}}{L_{L'e}}, \quad \left.\frac{\partial v_\theta}{\partial n}\right|_{\text{fluid}} = \frac{v_\theta|_e - v_\theta|_{L'}}{L_{L'e}} \tag{27}$$

The velocity components at L' and R' can be calculated by using bilinear interpolation or by using the gradient at the control volume center:

$$v_r|_{L'} = v_r|_L + (\text{grad}\, v_r)_L \cdot \mathbf{L'L} \tag{28}$$

4. RESULTS AND DISCUSSION

A dimensionless mesh size of $\frac{1}{200}$ was used to perform the simulations. The preliminary numerical tests with three different mesh sizes of $\frac{1}{100}$, $\frac{1}{200}$, and $\frac{1}{400}$ confirmed that the solutions based on mesh size of $\frac{1}{200}$ are grid independent.

Figure 3 presents typical flow field in the bioreactor with the scaffold. The rotating bottom-wall spins the fluid above it. The centrifugal force drives the fluid toward the side-wall. The fluid then spirals up along the side-wall. Turning the upper corner, the fluid converges toward the center along the free surface. Owing to the presence of the scaffold, some of the fluid changes its direction toward the axial region. Only a small portion of fluid passes through the scaffold. Below the scaffold, it is interesting that there is no wake or recirculation region. This is consistent with the experiment results of Dusting *et al.* [20].

There is a vortex breakdown bubble attached to the free surface at $Re = 1200$ (Figure 3(b)). The Reynolds number for onset of vortex breakdown is between $Re = 1000$ and 1200, which is higher than that in the bioreactor without the scaffold (about $Re = 500$) [21]. In addition, the size of the vortex breakdown bubble is smaller than that in the bioreactor without the scaffold. These

DOI: 10.1002/fld

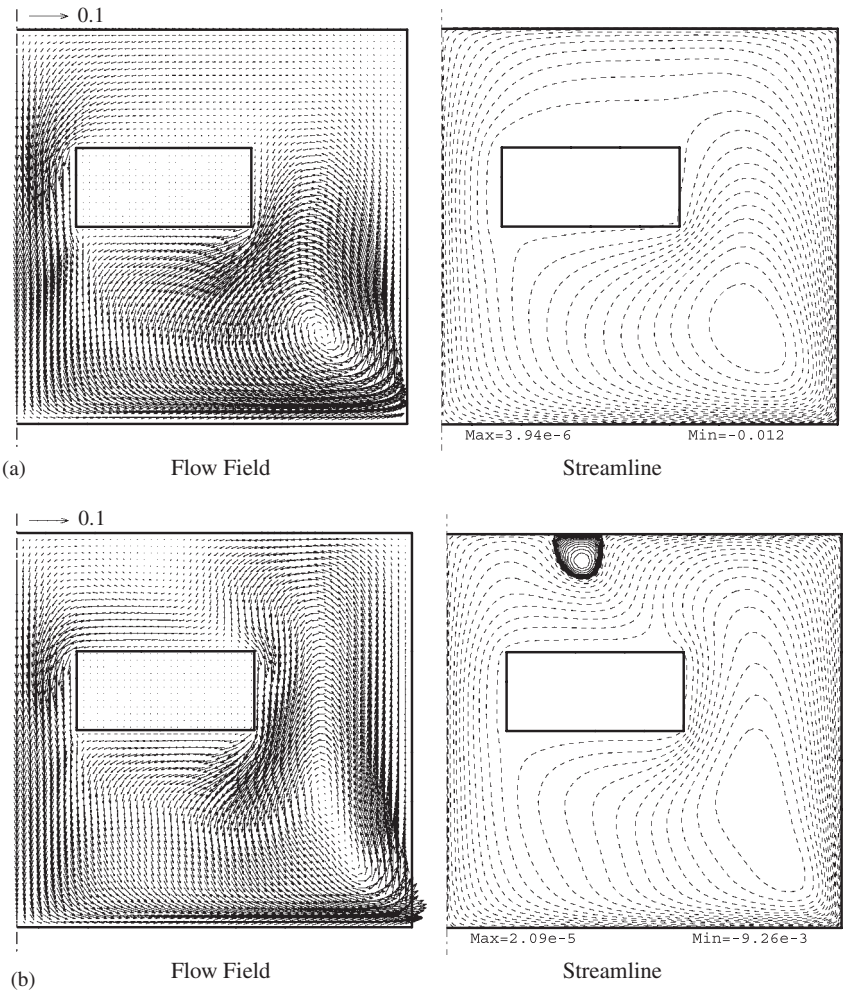

Figure 3. Flow fields and streamlines in the bioreactor at different Re; results obtained by the present code; $H/R=1$, $Dar=5\times10^{-6}$, $\varepsilon=0.6$: (a) $Re=500$ and (b) $Re=1200$; axisymmetric simulation. Contour levels C_i are non-uniformly spaced, with 25 positive levels $C_i=\text{Max(variable)}\times(i/25)^4$ and 25 negative levels $C_i=\text{Min(variable)}\times(i/25)^4$.

phenomena indicate that the presence of the scaffold hampers the formation of vortex breakdown. Another effect of the scaffold is to confine the vortex breakdown bubble to a region above the scaffold. Partly diverted by the vortex breakdown bubble, the fluid approaches the scaffold almost normally.

As shown in Figure 3, with an increase in Re, the recirculation region elongates toward the free surface. This means that more fluid is convected to the upper region and the velocity around the top surface of the scaffold becomes higher. The flow also approaches the scaffold differently at different Re. At a high Re (Figure 3(b)), the fluid moves toward the scaffold almost normally,

DOI: 10.1002/fld

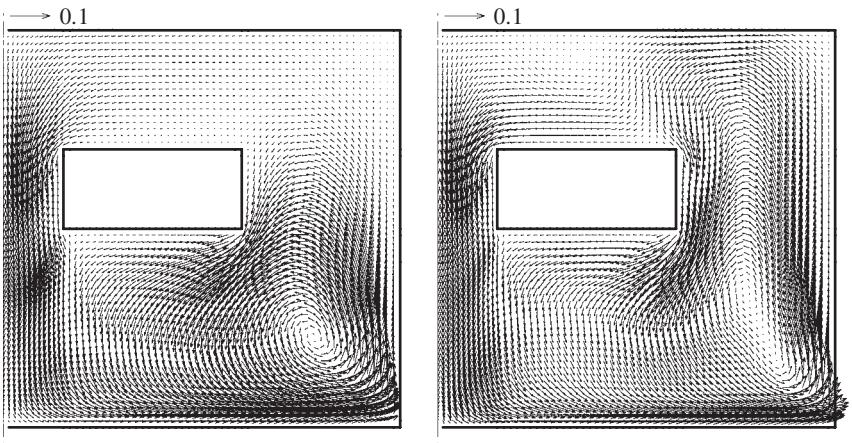

Figure 4. Flow fields in the bioreactor with an impermeable scaffold at different *Re*; three-dimensional simulation by FLUENT; $H/R=1$: (a) $Re=500$ and (b) $Re=1200$.

due to the presence of the vortex breakdown bubble, whereas at a low *Re* (Figure 3(a)), the flow approaches the scaffold more obliquely. In addition, at a high *Re* (Figure 3(b)) the flow divides at the top surface of the scaffold, whereas at a low *Re* (Figure 3(a)) the dividing point moves to the top right corner of the scaffold. These changes in the approaching flow with *Re* are attributed to the formation of a vortex breakdown bubble near the top surface.

For comparison, a full three-dimensional simulation was performed by using the commercial software FLUENT. An impermeable scaffold was used since the scaffold in the axisymmetric case had very small permeability with Darcy number (*Dar*) of 5×10^{-6}. It was confirmed that the three-dimensional simulation also gave axisymmetric flow. Figure 4 presents the flow fields in a vertical plane for the three-dimensional simulations, which appear rather similar to the axisymmetric results in Figure 3. In both simulations, the vortex breakdown bubble appears at high *Re* of 1200 and disappears at low *Re* of 500. The shape, size, and position of the bubble are also rather similar for both simulations. The axial velocity profiles along the axis are shown in Figure 5 for both simulations, and the discrepancy between them is small.

The porous flow pattern is related to the external flow pattern. At higher *Re*, the external flow pattern has shown that more fluid is convected to the upper region. In addition, the external flow approaches the scaffold less obliquely. Thus, more fluid passes through the scaffold, leading to a greater axial velocity at a higher *Re* (Figure 6). This trend has been clearly shown in Table II, which demonstrates that the axial component of velocity at the center of the scaffold becomes higher with an increase in *Re*. Figure 6 also shows that the porous flow at the right corner is especially stronger at $Re=1200$ than that at $Re=500$. The formation of the vortex breakdown bubble diverts some of the external flow to the right-hand side, thus causing an even higher velocity region there.

The porous flow at $Re=1200$ has a relatively larger radial velocity component toward the left-hand side than that at $Re=500$ (Figure 6; see also Table II). This is because more fluid is convected to the upper region at higher *Re*, as explained before. In addition, the presence of the nearby vortex breakdown bubble may lead to larger interface velocity at the top surface (Figure 3(b)).

DOI: 10.1002/fld

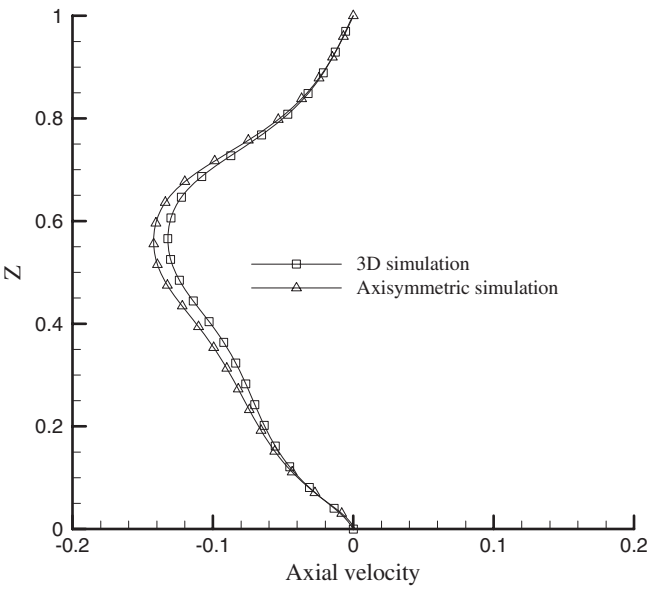

Figure 5. Axial velocity profiles along the axis in three-dimensional and axisymmetric simulations, $Re = 500$.

Figure 7 shows the pressure distributions along the scaffold surface at different *Re*. The pressures are presented with respect to that at the top of the axis. The pressure is high along the top surface and drops abruptly along the two side surfaces. The pressure is low along the bottom surface. At the dividing point (on top surface), the pressure is higher. Since only a small proportion of fluid can pass through the scaffold, the velocity at the dividing point decreases to a very small value, causing an increase in pressure according to the Bernoulli equation. Thus, the peak pressure is located at the top surface where the flow divides.

Figure 7 also shows that the pressure distribution changes much with the variation of *Re*. At a higher *Re*, the pressure at the top surface is higher and more non-uniform because the flow approaches the scaffold less obliquely (see Figure 3). With the flow at a more normal angle, the pressure drop between the top and right surfaces is also higher. There are other influences on the pressure distribution. The flow pattern changes at different *Re* due to the balance between the centrifugal force and the pressure gradient [22, 23]. The different flow patterns result in different pressure variations across streamlines and thus affect the pressure distribution on the scaffold surfaces.

The porous flow within the scaffold is much smaller than the surrounding flow (Figure 3). Thus, the swirling flow behavior, in particular the vortex breakdown phenomenon, seems to be mainly influenced by the chamber aspect ratio, the Reynolds number, the scaffold configuration, and the scaffold location. The effects of the permeability and porosity are secondary on vortex breakdown over the present range of parameters. However, the porous flow through the scaffold is significantly affected by the permeability as characterized by the Darcy number *Dar*. Table III clearly shows that the porous velocity is notably higher at a higher *Dar*. This is expected because a higher Darcy number means more porous flow for a certain pressure drop.

DOI: 10.1002/fld

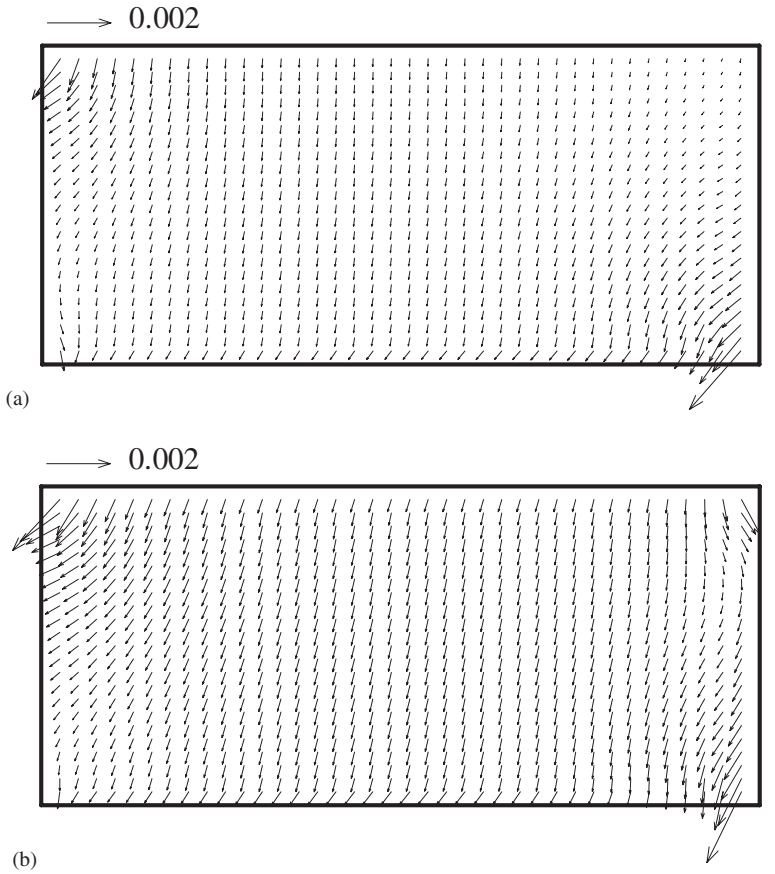

Figure 6. Flow fields within the scaffold in the bioreactor at different Re; $H/R=1$, $Dar=5\times10^{-6}$, $\varepsilon=0.6$: (a) $Re=500$ and (b) $Re=1200$.

Table II. Variation of velocity components at the center of the scaffold with Re ($H/R=1$, $Dar=5\times10^{-6}$, $\varepsilon=0.6$).

Re	Axial velocity (magnitude)	Radial velocity (magnitude)
500	2.41×10^{-4}	3.50×10^{-5}
1200	3.93×10^{-4}	9.14×10^{-5}

Figure 8 shows the pressure distributions along the scaffold surface at different Dar. The pressures are presented with respect to that at the top of the axis. The trends of pressure distributions are similar to those in Figure 7. The pressure is high along the top surface, drops abruptly along the two side surfaces, and is low along the bottom surface. There is a peak pressure on the top surface, associated with the dividing point (Figure 3).

DOI: 10.1002/fld

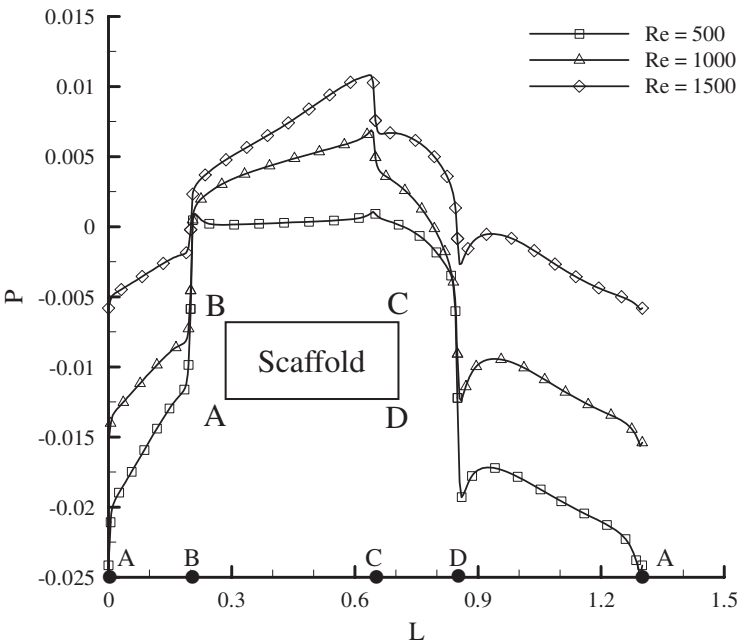

Figure 7. Pressure distributions along the scaffold surface for different *Re*; the reference pressure point is located at the top of the axis, where the pressure is assigned zero.

Table III. Variation of velocity components at the center of the scaffold with *Dar* ($H/R=1$, $Re=1000$, $\varepsilon=0.6$).

Dar	Axial velocity (magnitude)	Radial velocity (magnitude)
1×10^{-5}	6.84×10^{-4}	2.50×10^{-4}
1×10^{-6}	7.46×10^{-5}	2.48×10^{-5}
5×10^{-7}	3.68×10^{-5}	1.21×10^{-5}

The pressure distribution around the permeable scaffold is different from that of the solid one. The pressure drops between the top and side surfaces are slightly smaller for the permeable scaffolds, due to some of the flow being permitted to go through the scaffold. However, as discussed before, there are other complex influences on the pressure distribution. The flow pattern changes slightly at different *Dar* because the porous flow within the scaffold is different. The different flow patterns will give different pressure variations across streamlines and thus affect the pressure distribution for scaffolds with different permeabilities. These results indicate that it is important to couple the flows between the homogeneous region and porous medium regions, rather than treat them separately [19].

The results (Figure 8) also show that the variation of the permeability does not significantly change the pressure drop between the top and bottom surfaces. This pressure drop is the main driving force for the porous flow as it is mainly in the axial direction. From Darcy's law, if the

DOI: 10.1002/fld

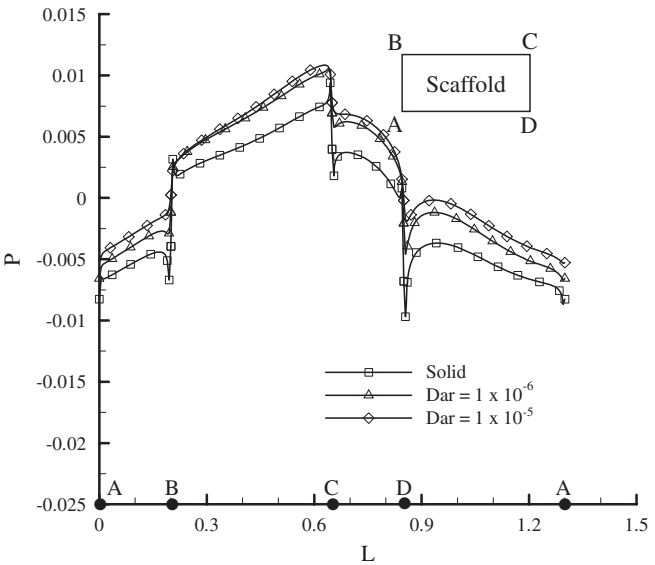

Figure 8. Pressure distributions along the scaffold surface for different *Dar*; the reference pressure point is located at the top of the axis, where the pressure is assigned zero.

Table IV. Variation of velocity components at the center of the scaffold with β_1 ($H/R=1$, $Re=1200$, $Dar=5\times10^{-6}$, $\varepsilon=0.6$, $\beta_2=0$).

β_1	Axial velocity (magnitude)	Radial velocity (magnitude)
-0.7	4.00×10^{-4}	9.49×10^{-5}
0	4.00×10^{-4}	9.43×10^{-5}
0.7	3.93×10^{-4}	9.14×10^{-5}

pressure drop is not changed, the average velocity within the scaffold is approximately proportional to the permeability. This explains why the porous velocity is higher at higher permeability (see Table III).

The jump parameters β_1 and β_2 used in the above simulations are fixed at 0.7 and 0, respectively. Previous studies (e.g. [13, 17, 18]) have shown that the jump parameters have some effect on velocity profile near the interface. As for the velocity in the bulk region of the scaffold, the present results indicate that the jump parameters have a small effect (see Table IV).

5. CONCLUDING REMARKS

The present study implements the interfacial stress-jump condition for a non-planar flow with three velocity components. The steady, laminar, Newtonian flow in a stirred micro-bioreactor with a porous scaffold inside was investigated. The present swirling flow is axisymmetric as the three velocity components are functions of only the axial and radial coordinates. As the technique is based

DOI: 10.1002/fld

on finite volume method with body-fitted and multi-block grids, the porous–fluid interface can be a non-flat surface. The present implementation can be extended to deal with a full three-dimensional situation by modifying the unit tangent vector.

For Reynolds number greater than 1200, a vortex breakdown bubble develops and attaches itself to the free surface. The scaffold delays the onset of vortex breakdown and confines the bubble to a region above the scaffold. The presence of the bubble results in a relatively larger radial velocity component within the scaffold. The Reynolds number has notable effects on the flow field both outside and inside the scaffold. The flow field outside the scaffold is not affected much by the variation in the permeability. However, the porous flow within the scaffold is higher at larger permeability. The pressure distributions along the scaffold surfaces are different for porous and solid cases. Thus, it is important to model the bioreactor flow system as a coupled flow involving porous medium and homogeneous fluid.

ACKNOWLEDGEMENTS

We wish to acknowledge Prof. Jim McGuirk of Loughborough University for his constructive remarks.

REFERENCES

1. Beavers GS, Joseph DD. Boundary conditions at a natural permeable wall. *Journal of Fluid Mechanics* 1967; **30**:197–207.
2. Neale G, Nader W. Practical significance of Brinkman's extension of Darcy's law: coupled parallel flows within a channel and a bounding porous medium. *Canadian Journal of Chemical Engineering* 1974; **52**:475–478.
3. Ochoa-Tapia JA, Whitaker S. Momentum transfer at the boundary between a porous medium and a homogeneous fluid, I: theoretical development. *International Journal of Heat and Mass Transfer* 1995; **38**:2635–2646.
4. Ochoa-Tapia JA, Whitaker S. Momentum transfer at the boundary between a porous medium and a homogeneous fluid, II: comparison with experiment. *International Journal of Heat and Mass Transfer* 1995; **38**:2647–2655.
5. Ochoa-Tapia JA, Whitaker S. Momentum jump condition at the boundary between a porous medium and a homogeneous fluid: inertial effect. *Journal of Porous Media* 1998; **1**:201–217.
6. Kuznetsov AV. Analytical investigation of the fluid flow in the interface region between a porous medium and a clear fluid in channels partially filled with a porous medium. *Applied Scientific Research* 1996; **56**:53–67.
7. Kuznetsov AV. Influence of the stress jump boundary condition at the porous-medium/clear-fluid interface on a flow at a porous wall. *International Communications in Heat and Mass Transfer* 1997; **24**:401–410.
8. Kuznetsov AV. Analytical investigation of Couette flow in a composite channel partially filled with a porous medium and partially with a clear fluid. *International Journal of Heat and Mass Transfer* 1998; **41**:2556–2560.
9. Partha MK, Murthy PVSN, Sekhar GPR. Viscous flow past a porous spherical shell—effect of stress jump boundary condition. *Journal of Engineering Mechanics* (ASCE) 2005; **131**:1291–1301.
10. Goyeau B, Lhuillier D, Gobin D, Velarde MG. Momentum transport at a fluid-porous interface. *International Journal of Heat and Mass Transfer* 2003; **46**:4071–4081.
11. Chandesris M, Jamet D. Boundary conditions at a planar fluid–porous interface for a Poiseuille flow. *International Journal of Heat and Mass Transfer* 2006; **49**:2137–2150.
12. Chandesris M, Jamet D. Boundary conditions at a fluid–porous interface: an *a priori* estimation of the stress jump coefficients. *International Journal of Heat and Mass Transfer* 2007; **50**:3422–3436.
13. Alazmi B, Vafai K. Analysis of fluid flow and heat transfer interfacial conditions between a porous medium and a fluid layer. *International Journal of Heat and Mass Transfer* 2001; **44**:1735–1749.
14. Gartling DK, Hickox CE, Givler RC. Simulation of coupled viscous and porous flow problems. *Computational Fluid Dynamics* 1996; **7**:23–48.
15. Costa VAF, Oliveira LA, Baliga BR, Sousa ACM. Simulation of coupled flows in adjacent porous and open domains using a control-volume finite-element method. *Numerical Heat Transfer A* 2004; **45**:675–697.
16. Betchen L, Straatman AG, Thompson BE. A nonequilibrium finite-volume model for conjugate fluid/porous/solid domains. *Numerical Heat Transfer A* 2006; **49**:543–565.

DOI: 10.1002/fld

17. Silva RA, de Lemos MJS. Numerical analysis of the stress jump interface condition for laminar flow over a porous layer. *Numerical Heat Transfer A* 2003; **43**:603–617.
18. Yu P, Lee TS, Zeng Y, Low HT. A numerical method for flows in porous and open domains coupled at the interface by stress jump. *International Journal for Numerical Methods in Fluids* 2007; **53**:1755–1775.
19. Sucosky P, Osorio FF, Brown JB, Neitzel GP. Fluid mechanics of a spinner-flask bioreactor. *Biotechnology and Bioengineering* 2004; **85**:34–46.
20. Dusting J, Sheridan J, Hourigan K. A fluid dynamic approach to bioreactor design for cell and tissue culture. *Biotechnology and Bioengineering* 2006; **94**:1197–1208.
21. Piva M, Meiburg E. Steady axisymmetric flow in an open cylindrical with a partially rotating bottom wall. *Physics of Fluids* 2005; **17**:063603.
22. Yu P, Lee TS, Zeng Y, Low HT. Effects of conical lids on vortex breakdown in an enclosed cylindrical chamber. *Physics of Fluids* 2006; **18**:117101.
23. Yu P, Lee TS, Zeng Y, Low HT. Characterization of flow behavior in an enclosed cylinder with a partially rotating end-wall. *Physics of Fluids* 2007; **19**:057104.
24. Cooper JA, Lu HH, Ko FK, Freeman JW, Laurencin CT. Fiber-based tissue-engineered scaffold for ligament replacement: design considerations and in vitro evaluation. *Biomaterials* 2005; **26**:1523–1532.
25. Galban CJ, Locke BR. Analysis of cell growth kinetics and substrate diffusion in a polymer scaffold. *Biotechnology and Bioengineering* 1999; **65**:121–132.
26. Li SH, de Wijn JR, Li JP, Layrolle P, de Groot K. Macroporous biphasic calcium phosphate scaffold with high permeability/porosity ratio. *Tissue Engineering* 2003; **9**:535–548.
27. Wang S, Tarbell JM. Effect of fluid flow on smooth muscle cells in a 3-dimensional collagen gel model. *Arteriosclerosis, Thrombosis, and Vascular Biology* 2000; **20**:2220–2225.
28. Hsu CT, Cheng P. Thermal dispersion in a porous medium. *International Journal of Heat and Mass Transfer* 1990; **33**:1587–1597.
29. Nithiarasu P, Seetharamu KN, Sundararajan T. Finite element modelling of flow, heat and mass transfer in fluid saturated porous media. *Archives of Computational Methods in Engineering* 2002; **9**:3–42.
30. Chen XB, Yu P, Winoto SH, Low HT. A numerical method for forced convection in porous and homogenous fluid domains coupled at interface by stress jump. *International Journal for Numerical Methods in Fluids* 2008; **56**:1705–1729.
31. Ferziger JH, Perić M. *Computational Methods for Fluid Dynamics* (2nd edn). Springer: Berlin, 1999.
32. Muzaferija S. Adaptive finite volume method for flow predictions using unstructured meshes and multigrid approach. *Ph.D. Thesis*, University of London, 1994.
33. van Doormal JP, Raithby GD. Enhancements of the SIMPLE method for predicting incompressible fluid flows. *Numerical Heat Transfer* 1984; **7**:147–163.
34. Rhie CM, Chow WL. Numerical study of the turbulent flow past an airfoil with trailing edge separation. *AIAA Journal* 1983; **21**:1525–1532.
35. Lilek Ž, Muzaferija S, Perić M, Seidl V. An implicit finite-volume method using nonmatching blocks of structured grid. *Numerical Heat Transfer B* 1997; **32**:385–401.

DOI: 10.1002/fld